The Response of Buoyant Coastal Plumes to Upwelling-Favorable Winds*

STEVEN LENTZ

Woods Hole Oceanographic Institution, Woods Hole, Massachusetts

(Manuscript received 24 February 2004, in final form 2 June 2004)

ABSTRACT

To better understand the response of a buoyant coastal plume to wind-induced upwelling, a two-dimensional theory is developed that includes entrainment. The primary assumption is that competition between wind-driven vertical mixing and lateral buoyancy forcing in the region where the isopycnals slope upward to intersect the surface results in continual entrainment at the offshore edge of the plume. The theory provides estimates of the buoyant plume characteristics and offshore displacement as a function of time t, given the wind stress, the characteristics of the buoyant plume prior to the onset of the wind forcing, and a critical value for the bulk Richardson number (Ri_c). The theory predicts that, for $\hat{t} \equiv t/t_s$, the plume density anomaly decreases as $(1 + \hat{t})^{-1}$, the thickness increases as $(1 + \hat{t})^{1/3}$, the width increases as $(1 + \hat{t})^{2/3}$, and the plume average entrainment rate decreases as $(1 + \hat{t})^{-2/3}$. Here $t_s = 2A_o/(\sqrt{\mathrm{Ri}_c}U_E)$ is the time for entrainment to double the cross-sectional area of the plume A_o at the onset of the wind forcing, where U_E is the Ekman transport. The theory reproduces results from 20 numerical model runs by Fong and Geyer, including their estimates of the plume-average entrainment rate (correlations greater than 0.98 and regression coefficients approximately 1 for plume characteristics and 1.7 for the entrainment rate). The theory, modified to allow for time-variable wind stress, also reproduces the observed response of the buoyant coastal plume from Chesapeake Bay during an 11-day period of upwelling winds in August 1994.

1. Introduction

Buoyant discharge from rivers or estuaries typically turns to the right (Northern Hemisphere) and forms a buoyant coastal plume that can flow tens to hundreds of kilometers alongshore before dispersing. Observational studies have shown that alongshore winds that oppose the buoyant coastal current (upwelling-favorable winds) can cause the buoyant water to separate from the coast, spread offshore, and eventually disperse if the winds are strong enough (Fong et al. 1997; Hickey et al. 1998; Rennie et al. 1999; Johnson et al. 2001; Sanders and Garvine 2001; Hallock and Marmorino 2002; Johnson et al. 2003). These studies suggest that upwelling-favorable wind forcing is the primary mechanism for the offshore dispersal of many buoyant coastal plumes. Therefore, determining the fate of various constituents, including the freshwater, discharged from rivers or estuaries and carried alongshore in buoyant coastal plumes requires an understanding of the response to upwelling-favorable winds (e.g., Lohrenz et al. 2003; McGillicuddy et al. 2003).

While numerical modeling studies have provided a qualitative characterization of the response of buoyant coastal plumes to upwelling-favorable winds (Chao 1988; Kourafalou et al. 1996; Xing and Davies 1999; Berdeal et al. 2002; Whitney and Garvine 2004), few studies have focused on the details of this process. A notable exception is Fong and Geyer (2001), who examined the response of an established buoyant coastal plume to upwelling-favorable winds using a primitive equation numerical model and also developed a conceptual model that provides considerable insight into this process. In their conceptual model, the buoyant water is carried offshore by the wind-driven Ekman transport in a layer of thickness h, and the plume eventually detaches from the coast. They estimate h using the wind stress, the density anomaly of the plume, and a bulk Richardson number criterion (Pollard et al. 1973; Trowbridge 1992). The bulk Richardson number criterion provides accurate estimates of the plume thickness when compared with results from the primitive equation numerical model. However, as noted by Fong and Geyer (2001), their estimate of h does not account for entrainment, though their analysis of the numerical model results clearly shows that entrainment is important.

Building on Fong and Geyer's results, a two-dimensional theory is developed here that explicitly includes entrainment and hence provides an estimate of the density, as well as the thickness, of the buoyant plume as

* Woods Hole Oceanographic Institution Contribution Number 11144.

Corresponding author address: Dr. Steve Lentz, MS21, Woods Hole Oceanographic Institution, Woods Hole, MA 02543.
E-mail: slentz@whoi.edu

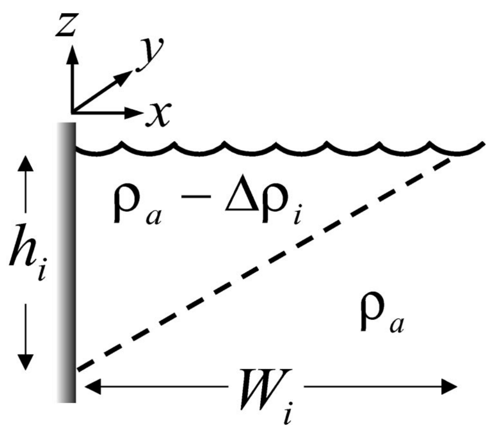

FIG. 1. Schematic of initial, two-dimensional buoyant coastal plume configuration prior to the onset of the wind.

it is transported offshore (section 2). The primary objective is to gain insight into the entrainment process and its implications for the buoyant plume response to upwelling-favorable winds. The proposed theory reproduces the basic features of the numerical model results of Fong and Geyer (2001), including their estimates of the plume-average entrainment rate (section 3). The theory also reproduces the basic features of the observed response to upwelling winds in August 1994 of the buoyant coastal plume that flows south from Chesapeake Bay (Rennie et al. 1999) (section 4).

2. Theory

The buoyant plume response to upwelling winds is assumed to proceed in three steps. First, the initial condition is that prior to the onset of an upwelling wind there is an established buoyant coastal plume with an alongshelf scale that is much larger than its width. Given this assumption, a two-dimensional theory is developed that neglects alongshelf variations. One consequence of this assumption is that the theory does not address the response of the source region to upwelling winds. Second, at the onset of the wind forcing there is immediate vertical mixing and entrainment over a portion of the plume. Third, the plume continues to evolve because of ongoing entrainment at the offshore edge of the plume.

a. Initial condition

Consider a buoyant plume of uniform density $\rho_a - \Delta\rho_i$ flowing along a vertical wall over an ambient fluid of density ρ_a prior to the onset of an upwelling-favorable wind stress (Fig. 1). (A subscript i refers to the initial plume characteristics prior to the onset of the wind). Assume for simplicity that the plume is two-dimensional, that is, no alongshore variations, with a triangular geometry such that the thickness is h_i at the wall and the width is W_i at the surface. A right-handed coordinate system is used with x positive offshore so that an upwelling-favorable wind is in the positive y direction.

b. Entrainment at the onset of wind forcing

At the onset of an upwelling-favorable alongshore wind stress τ^{sy}, assume a surface mixed layer forms at the offshore edge of the plume and deepens until there is a balance between wind-driven mixing and the stabilizing influence of the plume buoyancy such that the bulk Richardson number (Pollard et al. 1973) is a constant, Ri_c in the range 0.5–1.0 (Fig. 2). Thus,

$$\mathrm{Ri}_c = \frac{g\Delta\rho_o h_o}{\rho_a|\Delta u|^2}, \tag{1}$$

where g is gravitational acceleration, the buoyant plume has uniform density anomaly $\Delta\rho_o$ after the onset of the wind forcing and thickness h_o near the offshore edge of the plume, and $|\Delta u|$ is the velocity jump at the base

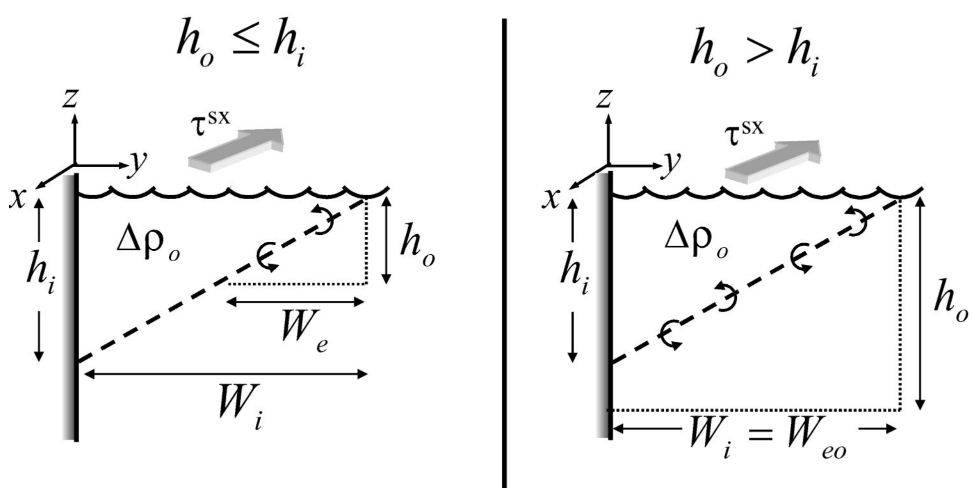

FIG. 2. Schematic of entrainment at the onset of the wind forcing for the cases (left) $h_o \leq h_i$ and (right) $h_o > h_i$.

of the plume. (A subscript o refers to the plume characteristics immediately after the onset of the wind forcing.) The primary contribution to $|\Delta u|$ is assumed to be from the wind-driven cross-shelf Ekman flow, which is estimated as the Ekman transport $U_E = \tau^{sy}/\rho_a f$ divided by h_o, where f is the Coriolis parameter (Fong and Geyer 2001). In the absence of wind forcing, the alongshore geostrophic shear in the buoyant coastal plume over a sloping bottom is assumed to be stable in a bulk Richardson number sense (Lentz and Helfrich 2002), and so this contribution to the vertical shear is neglected. Fong and Geyer's numerical model results and the comparisons in sections 3 and 4 support this assumption. Substituting U_E/h_o for $|\Delta u|$ and solving for h_o yields

$$h_o \approx \left(\frac{\mathrm{Ri}_c \rho_a U_E^2}{g\Delta\rho_o}\right)^{1/3}. \tag{2}$$

This is the expression derived by Fong and Geyer (2001) except that they assumed the density and velocity profiles in the plume were initially linear, which results in an additional factor of $4^{1/3}$ in their estimate of h_o. Note that both h_o and $\Delta\rho_o$ are not known because the entrainment that leads to h_o also decreases the plume density anomaly.

Here, and in the subsequent analysis, the plume density is assumed to be spatially uniform to simplify the analysis. Numerical model results and observations suggest that the plume density tends to be uniform because of a strong cross-shelf circulation within the plume that provides an exchange mechanism between the entrainment region and the rest of the plume (Fong and Geyer 2001; Houghton et al. 2004).

The plume density anomaly $\Delta\rho_o$ can be determined from buoyancy conservation given the cross-sectional area of the ambient fluid entrained into the plume. The cross-sectional area of the ambient fluid entrained into the plume immediately after the onset of the wind stress (A_{eo}) can be estimated for the simple triangular geometry chosen, assuming that entrainment only occurs in the region of the plume that is thinner than h_o (Fig. 2). Noting that the width of the entrainment region is $W_{eo} = W_i h_o/h_i$ when $h_o \le h_i$ and $W_{eo} = W_i$ when $h_o > h_i$,

$$A_{eo} \approx \begin{cases} W_{eo}h_o/2 = A_i\tilde{h}_o^2, & \tilde{h}_o \le 1 \\ A_i + W_i(h_o - h_i) = A_i(2\tilde{h}_o - 1), & \tilde{h}_o > 1, \end{cases} \tag{3}$$

where $A_i = W_i h_i/2$ is the initial cross-sectional area of the plume, and $\tilde{h}_o = h_o/h_i$ is the normalized thickness at the offshore edge of the plume. Thus, the cross-sectional area of the plume after the onset of the wind $A_o = A_i + A_{eo}$ is

$$A_o \approx \begin{cases} A_i(1 + \tilde{h}_o^2), & \tilde{h}_o \le 1 \\ 2A_i\tilde{h}_o, & \tilde{h}_o > 1. \end{cases} \tag{4}$$

Conservation of buoyancy implies that

$$\Delta\rho_o A_o = \Delta\rho_i A_i. \tag{5}$$

Since the right-hand side is fixed by the initial conditions, the subsequent plume cross-sectional area and density anomaly are inversely proportional to each other. Using (4) to eliminate A_o and solving for $\Delta\rho_o$ yields

$$\Delta\rho_o \approx \begin{cases} \Delta\rho_i(1 + \tilde{h}_o^2)^{-1}, & \tilde{h}_o \le 1 \\ \Delta\rho_i(2\tilde{h}_o)^{-1}, & \tilde{h}_o > 1. \end{cases} \tag{6}$$

An equation for $\tilde{h}_o$ may be obtained by substituting (6) into (2):

$$\begin{cases} \tilde{h}_o^3 - \tilde{h}_s^2(\tilde{h}_o^2 + 1)/2 \approx 0, & \tilde{h}_s \le 1 \\ \tilde{h}_o \approx \tilde{h}_s, & \tilde{h}_s > 1, \end{cases} \tag{7}$$

where $\tilde{h}_s = h_s/h_i$,

$$h_s = \left(\frac{2\mathrm{Ri}_c \rho_a U_E^2}{g h_i \Delta\rho_i}\right)^{1/2}, \tag{8}$$

and $\tilde{h}_s = 1$ when $\tilde{h}_o = 1$ has been used to express the range of validity for the two equations in (7) in terms of $\tilde{h}_s$ rather than $\tilde{h}_o$. The normalized thickness scale $\tilde{h}_s$ only depends on the initial plume characteristics and the wind stress. It may be thought of as a Froude number, in this case, the Ekman velocity U_E/h_i divided by the internal wave speed $\sqrt{g_i' h_i}$, where $g_i' = g\Delta\rho_i/\rho_a$. The magnitude of $\tilde{h}_s$ determines the plume response to the onset of the wind stress. If $\tilde{h}_s \ge 1$, the wind forcing is strong enough for entrainment to occur over the entire extent of the plume and the plume thickness at the onset of the wind forcing is h_s. If $\tilde{h}_s < 1$, only a portion of the plume is thin enough for entrainment to occur, and the plume thickness at the onset of the wind forcing is larger than h_s.

It is straightforward to show that the cubic for $\tilde{h}_s \le 1$ always has one real root and a complex conjugate pair (Selby 1973). The solution for the cubic is complicated and therefore the real root is found numerically in the following analysis. The density anomaly $\Delta\rho_o$ can be determined by substituting the solution to (7) into (6). The estimates above, and in the following section, are approximate because of the oversimplified plume geometry, the deformation radius scaling, and uncertainty in Ri_c.

c. *Continual entrainment at the offshore edge of the plume*

After the onset of the wind, Fong and Geyer's numerical model results indicate that there continues to be entrainment of ambient shelf water into the buoyant plume (see their Fig. 12). This continual entrainment causes the cross-sectional area (volume) of the plume to increase and the density anomaly to decrease. The decreasing density anomaly and (2) implies an increasing plume thickness. In the numerical model results the entrainment is concentrated near the offshore edge of the plume, in the region where the plume interface

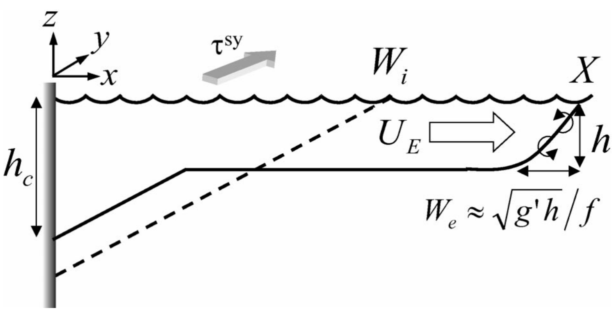

FIG. 3. Schematic of wind-driven entrainment at the offshore edge of the buoyant plume. The entrainment is assumed to be the result of a competition between geostrophic adjustment associated with the buoyancy forcing and wind-driven mixing in the region where the isopycnals slope upward to intersect the surface. The width of this region is assumed to scale with the baroclinic deformation radius. The dashed line shows the initial shape of the plume as depicted in Fig. 1.

shoals. Entrainment presumably occurs because the plume is thinner in this region than the equilibrium thickness given by the bulk Richardson number criterion. This entrainment is assumed here to be the result of a competition between wind-driven mixing that tends to steepen the isopycnals and the cross-shelf buoyancy flux that tends to relax the isopycnals toward a geostrophically adjusted state (Fig. 3). For simplicity, consider this as a two-step process in which there is first a geostrophic adjustment over a time scale of f^{-1}. This implies that the width of the region of sloping isopycnals, where the entrainment occurs, scales with the baroclinic deformation radius $W_e \approx \sqrt{g'h}/f$, where $g' = g\Delta\rho/\rho_a$. This is followed by wind-driven vertical mixing that satisfies the bulk Richardson criterion as in (1); that is,

$$h \approx \left(\frac{\mathrm{Ri}_c \rho_a U_E^2}{g\Delta\rho}\right)^{1/3}, \tag{9}$$

where $h(t)$ and $\Delta\rho(t)$ are the time-dependent plume thickness and density anomaly. The wind mixing and geostrophic adjustment actually occur simultaneously, but this perspective suggests plausible time f^{-1} and width W_e scales for the entrainment process. As noted earlier, a critical element of this scenario is a circulation within the plume that constantly exchanges fluid between the entrainment region and the rest of the plume to maintain a spatially uniform density (Fong and Geyer 2001; Houghton et al. 2004). The cross-sectional area of the entrained fluid A_e is approximately $W_e h/2$, and the rate at which the plume area increases is

$$\frac{\partial A}{\partial t} \approx A_e f = \frac{\sqrt{g'h}h}{2f} f = \frac{1}{2}\left(\frac{g\Delta\rho h^3}{\rho_a}\right)^{1/2}. \tag{10}$$

Substituting h from (9) into (10) yields

$$\frac{\partial A}{\partial t} \approx \frac{1}{2}\sqrt{\mathrm{Ri}_c} U_E. \tag{11}$$

Integrating from $t' = 0$ (just after the onset of the wind) to $t' = t$ for a constant wind stress provides an expression for the time-dependent cross-sectional area

$$A = A_o(1 + \hat{t}), \tag{12}$$

where A_o is the cross-sectional area after the onset of the wind stress given by (4) and $\hat{t}$ is t normalized by $t_s = 2A_o/(\sqrt{\mathrm{Ri}_c} U_E)$. From (12), t_s is the time it takes entrainment to double the cross-sectional area from A_o to $2A_o$ or equivalently, from buoyancy anomaly conservation

$$\Delta\rho A = \Delta\rho_o A_o, \tag{13}$$

to reduce the density anomaly by a factor of 2. Substituting A from (12) into (13) yields

$$\Delta\rho = \Delta\rho_o(1 + \hat{t})^{-1}. \tag{14}$$

Substituting (14) into (9) and using (2) yields

$$h = h_o(1 + \hat{t})^{1/3}. \tag{15}$$

The cross-shelf position of the offshore edge of the plume $X(t)$ may be estimated by integrating in time the Ekman transport U_E divided by the plume thickness h. Noting that $X(t = 0) = W_i$ and, assuming the wind stress is constant, this yields

$$X = W_i + \int_0^t \frac{U_E}{h}\,dt$$

$$= W_i + \frac{3A_o}{\sqrt{\mathrm{Ri}_c} h_o}[(1 + \hat{t})^{2/3} - 1]. \tag{16}$$

Estimates of the plume width $W(t)$ depend on the character of the cross-shelf divergence of the Ekman transport near the coast. In the following, the onshore portion of the plume that is thicker than h is assumed to shoal while maintaining the initial interface slope (h_i/W_i) (Fig. 3). This is qualitatively consistent with the response to onshore flow in the lower layer that is compensating for the near-surface offshore transport. The plume is assumed to separate from the coast when the plume thickness at the coast (h_c) equals h. An alternate model in which the divergence is concentrated at the coast (vertical wall) was also considered. In this case, the plume immediately separates from the coast. This model is probably more appropriate for the case where the coast is a vertical wall and the lower layer is much thicker than the plume. The two models give very similar results in the evaluations presented in sections 3 and 4. Only the former case is presented here because it seems more relevant to the oceanic case and it provides an estimate of the time it takes the plume to separate from the coast. Separation from the coast is important because the plume should no longer propagate alongshore once it has separated from the coast (though it may be advected alongshore by the ambient shelf flow).

Separation from the coast occurs when $h_c = h$, which implies $A = Xh$. Using (12), (15), (16) and solving for the time t_{sep} when $A = Xh$ yields

$$\tilde{t}_{\text{sep}} = \begin{cases} \left(\dfrac{3 - \sqrt{\text{Ri}_c}\tilde{h}_s^2/\tilde{h}_o^2}{3 - \sqrt{\text{Ri}_c}}\right)^{3/2} - 1, & \tilde{h}_s \le 1 \\ 0, & \tilde{h}_s > 1, \end{cases} \quad (17)$$

where (4) and (7) have been used to simplify this expression and $\tilde{t}_{\text{sep}} = t_{\text{sep}}/t_s$. The normalized separation time $\tilde{t}_{\text{sep}}$ is only a function of $\tilde{h}_s$ and Ri_c since $\tilde{h}_o$ is only a function of $\tilde{h}_s$. For $\text{Ri}_c = 1$, $\tilde{t}_{\text{sep}}$ decreases from about 0.85 to 0 as $\tilde{h}_s$ goes from 0 to 1. Thus, the separation time t_{sep} is always less than the entrainment doubling time scale t_s. However, both t_s and t_{sep} are inversely proportional to the wind stress for small $\tilde{h}_s$, and so both time scales increase as the wind stress approaches zero.

If the plume has separated from the coast or $h_o > h_i$ (Fig. 2, right panel), then the plume cross section is assumed to be rectangular and $W = A/h$. If the plume has not separated from the coast, then $W = X$. Using (12), (15), and (16), the width W is

$$W = \begin{cases} X = W_i + \dfrac{3U_E t_s}{2h_o}[(1 + \hat{t})^{2/3} - 1], & \tilde{h}_s \le 1 \\ & t \le t_{\text{sep}} \\ \dfrac{A}{h} = W_i\left(\dfrac{h_s}{h_o}\right)^2(1 + \hat{t})^{2/3}, & \tilde{h}_s \le 1 \\ & t > t_{\text{sep}} \\ \dfrac{A}{h} = W_i(1 + \hat{t})^{2/3}, & \tilde{h}_s > 1 \\ & t > 0. \end{cases} \quad (18)$$

As discussed in the following section, Fong and Geyer (2001) made estimates of the plume-average entrainment rate $\overline{w}_e$ for each of the numerical model runs. For comparison, the plume-average entrainment rate from the theory may be estimated as

$$\overline{w}_e = \frac{1}{W}\frac{\partial A}{\partial t}, \quad (19)$$

using (18) and (11). Once the plume has separated from the coast, the entrainment rate decreases as $(1 + \hat{t})^{-2/3}$. Since the entrainment only occurs over a small portion of the plume, $\overline{w}_e$ is much smaller than the local entrainment at the offshore edge of the plume, which from (11) is

$$w_e \approx \frac{1}{W_e}\frac{\partial A}{\partial t} = \frac{1}{2}hf = \frac{1}{2}h_o f(1 + \hat{t})^{1/3}. \quad (20)$$

Note that the local entrainment rate actually increases with time because the plume density anomaly is decreasing.

Equations (14), (15), (16), (18), and (19) provide estimates of the time-dependent plume characteristics in response to upwelling-favorable winds that depend only on the initial buoyant coastal plume characteristics ($\Delta\rho_i$, h_i, and W_i), latitude (f), wind stress, and the choice of Ri_c.

3. Comparison with numerical model results

Fong and Geyer (2001) used a primitive equation numerical model with a turbulent closure scheme that depends on the stratification and the current shear (Mellor–Yamada level 2.5; Mellor and Yamada 1982) to investigate the buoyant coastal plume response to upwelling-favorable winds. In each of the model runs a buoyant discharge at the coast forms a buoyant coastal plume, which was allowed to spin up for 36 days. After 36 days a constant, upwelling-favorable wind stress was applied. Twenty model runs were made in which they varied the wind stress, the freshwater transport at the source, and the depth of the source. The latter two parameters caused variations in the initial buoyant coastal plume characteristics h_i and $\Delta\rho_i$ ($\overline{h}_o$ and $\overline{\Delta\rho}_o$ in Table 1 of their paper). They provide estimates of h for 15 of the model runs and $\Delta\rho$ for 14 of the model runs 72 h after the onset of the wind stress (h_s and $\overline{\Delta\rho}_s$ in Table 2 of their paper). They do not list estimates for the other model runs because the density anomaly was too small (<0.5 kg m^{-3}) to accurately determine h or $\Delta\rho$. Fong and Geyer (2001) also present a sequence of salinity sections from three of the numerical model runs (wind stresses of 0.05, 0.1, 0.2 Pa; Figs. 7 and 10 in their paper) at four different times after the onset of the wind stress (12, 24, 48, and 72 h) that allow estimation of the cross-shelf position of the offshore edge of the plume $X(t)$ and the plume width $W(t)$. Last they made estimates of the plume-averaged entrainment rate $\overline{w}_e$, 72 h after the onset of the wind for all 20 numerical model runs (Fig. 13 in their paper).

Estimates of the wind-driven plume thickness h from (15), $\Delta\rho$ from (14), W from (18), X from (16), and $\overline{w}_e$ from (19) are made using the parameters and initial plume conditions prior to the onset of the wind forcing for the numerical model calculations of Fong and Geyer (2001). Specifically, the input parameters are $f = 10^{-4}$ s^{-1}, $\rho_a = 1025.4$ kg m^{-3} (ambient salinity 32 and temperature 4°C), $W_i = 25$ km, and τ^w, $\overline{h}_o$, and $\overline{\Delta\rho}_o$ are from their Table 1, where $h_i = 2\overline{h}_o$, because $\overline{h}_o$ is the average initial plume thickness, and $\Delta\rho_i = \overline{\Delta\rho}_o$. The critical bulk Richardson number Ri_c is assumed to be 1.0 in all subsequent analyses. The theoretical estimates are scalings, with assumed $O(1)$ coefficients that presumably depend on factors such as the actual geometry of the plume and entrainment regions, which are not triangular; initial stratification within the plume; the relationship between the width of the entrainment region at the offshore edge of the plume and the baroclinic deformation radius; and the critical value of the bulk Richardson number.

In general, there is close agreement between the theoretical predictions and the numerical model results (Table 1 and Figs. 4–6), with correlations greater than 0.98 and regressions slopes that range from 1 to 1.7. The estimates of the plume thickness h from (15) are very similar to Fong and Geyer's estimates using the ob-

TABLE 1. Results of linear regression analyses of the form $x = ax_{\mathrm{num}} + b$, where x is the estimate of the variable in column 1 from the theory and x_{num} is the corresponding estimate from the numerical model results. All correlations are significant at the 99% confidence level, and 95% confidence intervals for the slopes a and intercepts b are listed. Corresponding comparisons are shown in Figs. 4 and 6.

Variable	Intercept	Slope	Correlation	Data points
h	-1.60 ± 0.64	1.25 ± 0.10	0.990	15
$\Delta\rho$	-0.24 ± 0.17	1.04 ± 0.13	0.982	14
X	1.03 ± 2.90	1.06 ± 0.06	0.996	12
W	-7.75 ± 4.30	1.33 ± 0.11	0.992	12
$\overline{w}_e$	-0.10 ± 0.16	1.66 ± 0.14	0.985	20

served density anomaly (Fig. 4a). (Fong and Geyer present estimates for both $\mathrm{Ri}_c = 0.5$ and $\mathrm{Ri}_c = 1.0$; the former are shown in Fig. 4a to better match the numerical model results.) Relative to the numerical model results, the theory underestimates h for small values ($h < 8$) and overestimates h for larger values. The predicted plume densities from (14) are all slightly less than the plume densities from the numerical model results (Fig. 4b). This discrepancy may be partially due to the plume being defined as salinities less than 31.5

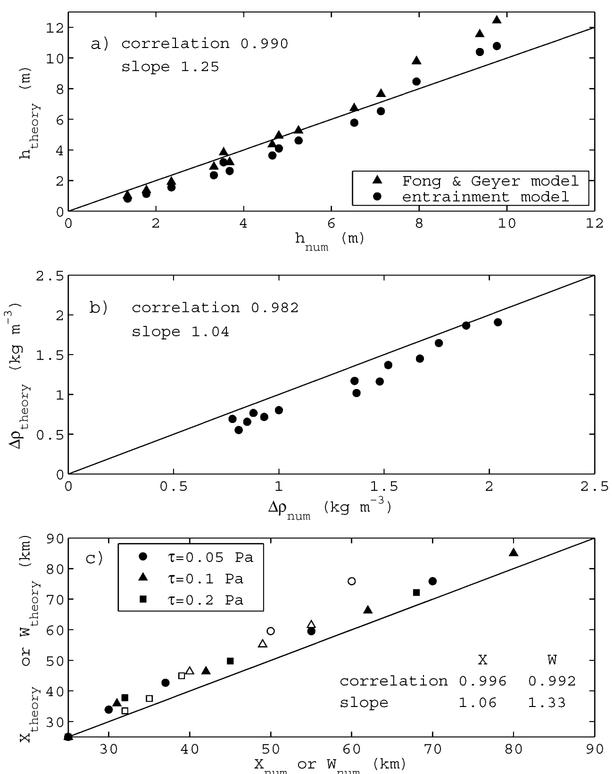

FIG. 4. Comparisons of numerical model estimates with theoretical estimates of (a) plume thickness h estimated from (15), (b) density anomaly $\Delta\rho$ estimated from (14), and (c) width W estimated from (18) (open symbols) and the offshore edge of plume X estimated from (16) (solid symbols). Estimates of h from Fong and Geyer (2001) for $\mathrm{Ri}_c = 0.5$ are also shown (squares) in (a). Results in (c) are for three numerical model runs with different wind stress magnitudes. For reference, a line with a slope of 1.0 is shown in each frame.

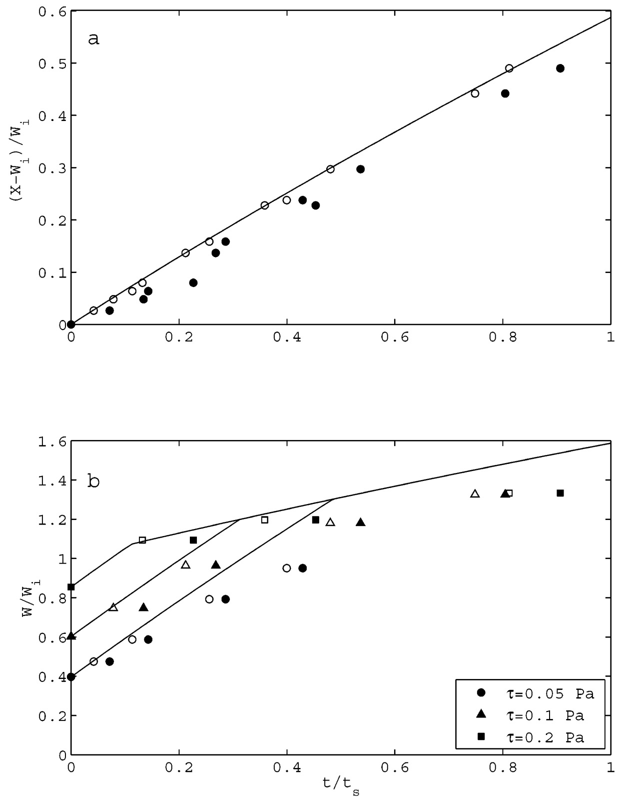

FIG. 5. (a) The normalized offshore position of the plume $(X - W_i)/W_i$ and (b) width W/W_i as a function of the normalized time t/t_s. In both cases the lines represent the theoretical estimates (16) and (18), and the symbols represent the numerical model results for wind stresses of 0.05, 0.1, and 0.2 Pa. The open symbols are the numerical model run results shifted 5 h earlier (before normalizing) to account for Ekman spinup time and the ramping up of the wind stress.

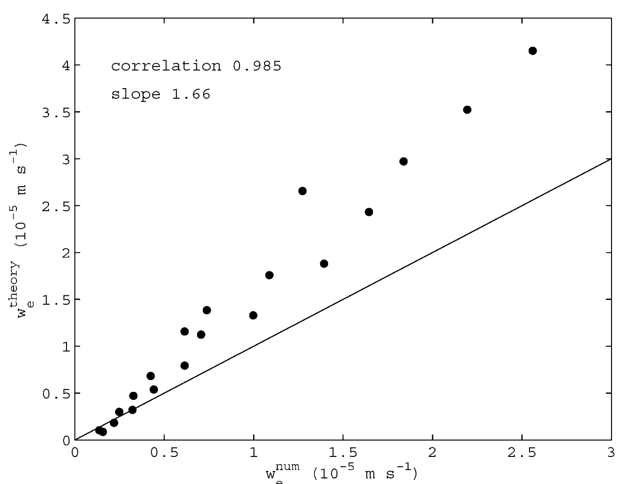

FIG. 6. Comparisons of plume-average entrainment rates 72 h after the onset of the wind forcing estimated from the 20 numerical model runs of Fong and Geyer (2001), w_e^{num}, and from (19), w_e^{theory}. A line with a slope of 1.0 is shown for reference.

in the analysis of the numerical model results, even though the ambient salinity is 32. Therefore, $\Delta\rho$ estimates from the numerical model results are a slight overestimate of the plume density anomaly. However, the discrepancy is also consistent with the entrainment rate estimated from the theory being larger than the numerical model estimates (Fig. 6).

The theory slightly overestimates X and W relative to the numerical model results (Fig. 4c). The offshore position of the plume from the numerical model, normalized as in (16) and plotted against normalized time $\hat{t}$, both collapses the numerical model results and agrees reasonably well with the theory (Fig. 5a solid circles). Note that the three 72-h numerical model runs used in the temporal comparisons of X and W only span normalized times that are less than 1. The theoretical estimates lead the numerical model estimates. Two factors probably contribute to this. First, the wind stress in the numerical model was ramped up over 1.7 h (D. Fong 2003, personal communication), which was not accounted for in the theoretical estimates. Second, the theory assumes an instantaneous Ekman response; that is, it ignores the spinup time of roughly $f^{-1} \approx 2.8$ h. There is closer agreement in the temporal responses if the numerical estimates are first shifted by 5 h to crudely account for these two factors (Fig. 5a, open circles). The normalized widths from (18) as a function of normalized time also agree reasonably well with the theory (Fig. 5b). At short times, $\hat{t} < 0.5$, the theory and numerical model results do not collapse to one curve because they have been normalized by the long-time solution from (18). Shifting the numerical model results by 5 h also improves the comparison for W.

Average entrainment rates from the theory are well correlated with the numerical model estimates, but are about 1.7 times as large. Variations in the Ri_c between 0.5 and 1.5 do not change this regression slope appreciably. Given the uncertainties in the accuracy of turbulence closure schemes, it is unclear which of the two estimates is more accurate. It is also difficult to accurately estimate the plume-average entrainment rate, even given numerical model results (Fong and Geyer 2001). However, the linear relationship between the theoretical and numerical model estimates of $\overline{w}_e$ is encouraging and suggests that the entrainment process in the numerical model is essentially what is outlined in the theory. In particular, the entrainment is not one-dimensional, but is concentrated near the offshore edge of the plume. This theoretical estimate is much closer to the numerical estimates than the bulk Richardson number scaling proposed by Fong and Geyer (2001) based on one-dimensional entrainment studies. The concentration of the entrainment over a small portion of the plume also explains why the comparison with the one-dimensional scalings yielded a proportionality coefficient that was substantially smaller than in previous studies.

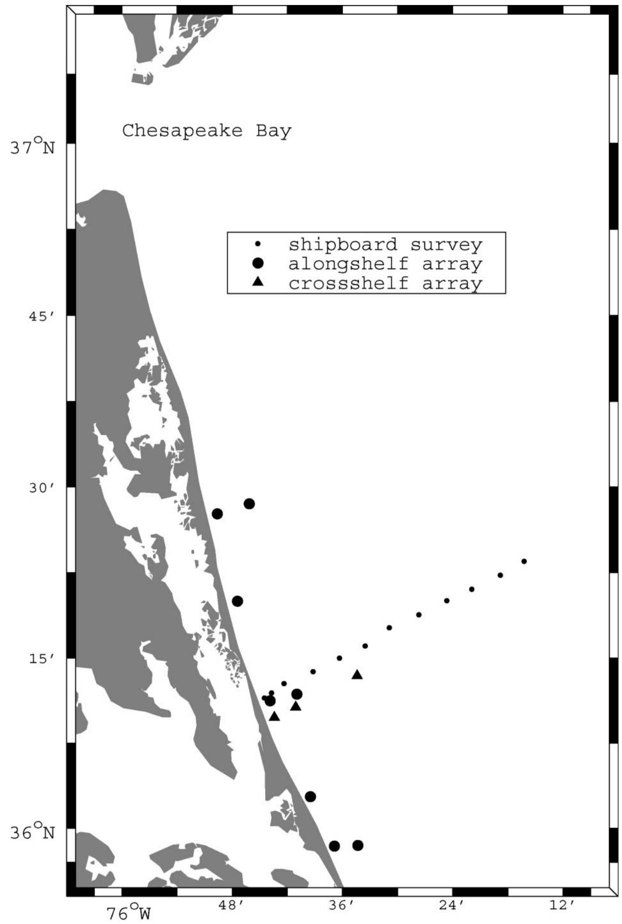

FIG. 7. Map showing locations of ship survey stations and moored arrays from 1994 inner-shelf study. Symbols along central line have been shifted slightly for clarity.

4. Chesapeake buoyant coastal plume characteristics

Observations of the response of the buoyant coastal plume emanating from Chesapeake Bay to upwelling-favorable winds are used to further evaluate the theoretical ideas proposed in section 2. Hydrographic observations of the buoyant coastal plume were obtained in August and October 1994 from repeated cross-shelf ship transects near Duck, North Carolina, approximately 100 km south of Chesapeake Bay (Waldorf et al. 1995, 1996) (Fig. 7). Alongshelf and cross-shelf arrays of moored instruments were deployed at the same site from August through November 1994 (Alessi et al. 1996; Lentz et al. 1999). The alongshelf arrays consisted of temperature, conductivity, and pressure sensors deployed at five sites along the 5-m isobath with 15-km spacing and three sites along the 20-m isobath with 30-km spacing, centered at the cross-shelf array, about 100 km south of Chesapeake Bay. The cross-shelf array consisted of conductivity (salinity), temperature, and current measurements spanning the water column at sites

0.4, 0.9, 1.6, 5.4, and 16.4 km offshore (water depths 4, 8, 13, 21, and 26 m, respectively). Wind stresses were estimated (Large and Pond 1981) using wind measurements from the end of the U.S. Army Corps of Engineers Field Research Facility pier. Winds in this area have a correlation scale of about 600 km and thus winds at the pier are representative of winds over the buoyant coastal plume (Austin and Lentz 1999). Previous studies using these observations have provided a general description of the buoyant coastal plume (Rennie et al. 1999) and a more detailed description of the region near the nose (Lentz et al. 2003).

Releases of buoyant water from Chesapeake Bay are controlled by wind-driven sea level fluctuations at the mouth of the bay (Wang 1979; Rennie et al. 1999) and result in intermittent buoyant coastal plumes that often propagate more than 100 km southward along the coast (Rennie et al. 1999; Johnson et al. 2001; Donato and Marmorino 2002; Lentz et al. 2003). In August and October 1994, the resulting buoyant coastal plumes propagated at about 0.5 m s^{-1} along the coast and were typically about 5 km wide. Upwelling-favorable winds are a primary mechanism causing the offshore dispersal of the buoyant coastal plume from Chesapeake Bay (Rennie et al. 1999; Johnson et al. 2001; Hallock and Marmorino 2002). In 1994, weak upwelling-favorable wind stresses (<0.1 Pa) were associated with the disappearance of the buoyant plume from the sites near the coast in 14 of 17 buoyant coastal plume events. In the other three events, the plume decayed alongshore, apparently as a result of vertical mixing associated with strong downwelling-favorable wind stresses (magnitudes > 0.2 Pa). In the upwelling cases, the salinity increase occurred more or less simultaneously over the 60-km extent of the alongshelf array and there was clear evidence of the buoyant water moving offshore. At the onset of upwelling-favorable winds, salinity increases at the 13-m site (1.6 km offshore) preceded or were simultaneous with the appearance of the low-salinity water first at the 21-m site (5.4 km offshore) and in about one-half of the cases subsequently at the 26-m site (16.4 km offshore) (e.g., 17 August and 21 August events in Fig. 8). The salinity anomaly decreased with distance offshore and was generally small at the 26-m site, suggesting mixing with the ambient shelf water.

A sequence of salinity sections from the ship surveys shows an example of the evolution of the low-salinity plume water as it is carried offshore (Fig. 9) during a 12-day period in August when winds were generally upwelling favorable (Fig. 8a). From 7 to 9 August, winds were downwelling favorable and there was a buoyant coastal plume present at the mooring transect. Winds were weak on 10–11 August and the buoyant plume was about 10 m thick and less than 10 km wide (Fig. 9). As a result of weak upwelling-favorable winds the plume thinned and spread offshore by 12 August with relatively little change in salinity. By 14 August, in response to stronger upwelling-favorable winds, the plume is more than 20 km wide and has begun to separate from the coast, and the plume salinity has increased. A second buoyant plume propagates into the region late on 16 August during a period of weak winds, and then moves offshore and apparently merges with the low-salinity water from the previous event during the upwelling wind event on 17–18 August (Fig. 8). By 19 August the core of the low-salinity water is 30–40 km offshore and the plume is about 10 m thick. A third buoyant coastal plume event occurs 20–21 August (Fig. 8) and is immediately swept about 10 km offshore by the upwelling-favorable winds (Fig. 9). The remnant of the older merged plume is still evident 30–40 km offshore on 21 August. Downwelling-favorable winds on 23 August cause both plumes to move onshore and the salinity to increase because of vertical mixing. These observations indicate that weak to moderate upwelling-favorable winds are an effective mechanism for dispersing the buoyant coastal plume offshore.

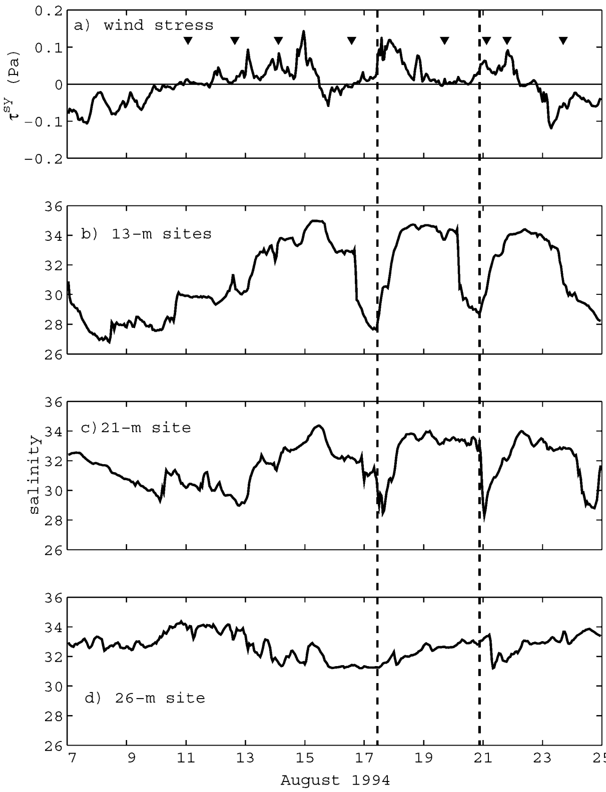

FIG. 8. Time series from 7 to 25 Aug 1994 of (a) wind stress, and near-surface salinities at mooring sites (b) 1.3, (c) 5.6, and (d) 16 km offshore. Onset of two upwelling-favorable (positive) wind stress events is marked by dashed lines. Times of shipboard transects shown in Fig. 9 are noted by triangles in (a). Buoyant coastal plume events are evident in (b) on 7–11, 16–17, and 20 Aug.

It is interesting that the buoyant water could be tracked for an extended period of time after it separated from the coast (Fig. 9), suggesting that it persisted as a coherent lens of low-salinity water and did not break up. Additional hydrographic observations from lines

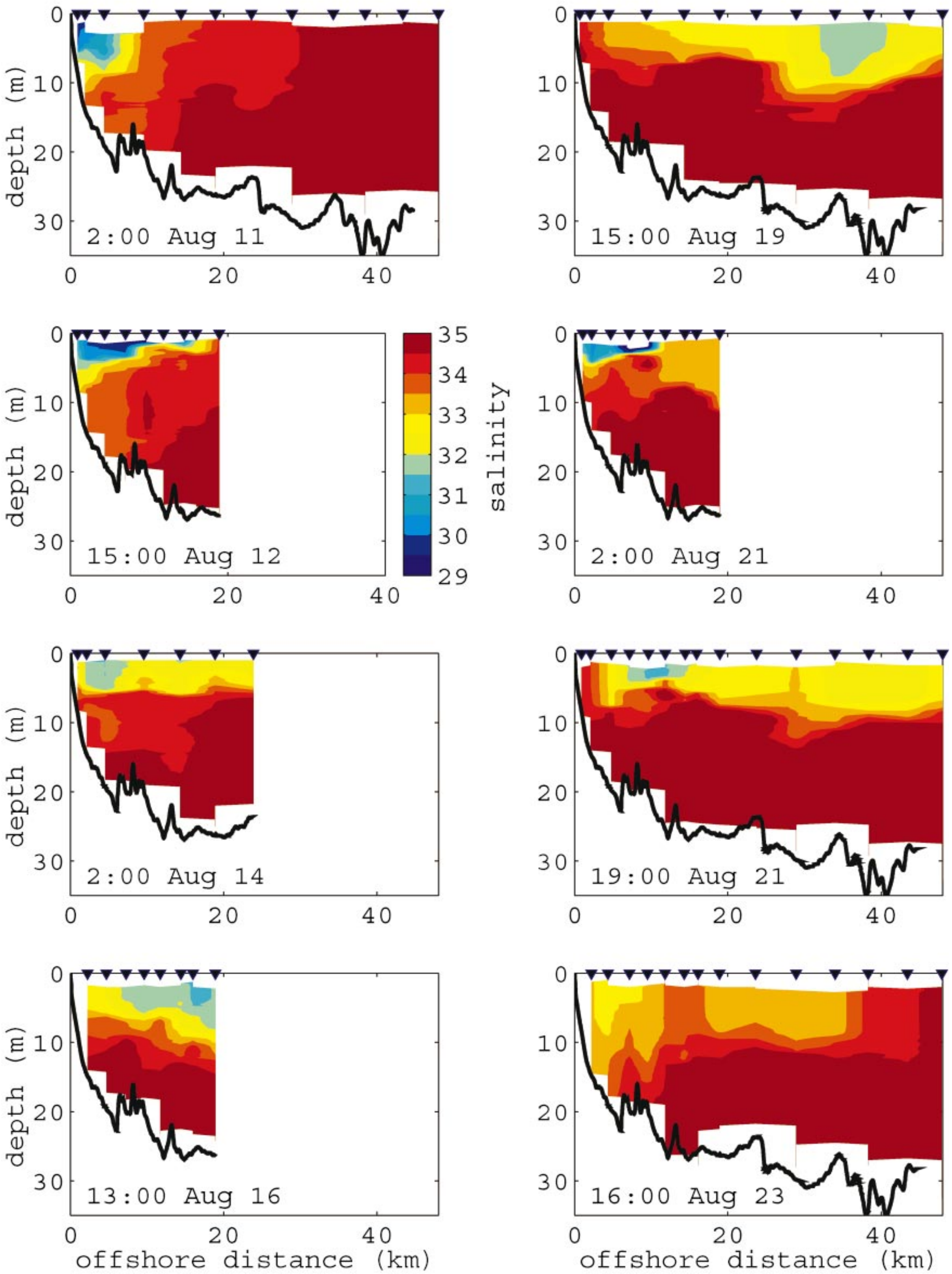

FIG. 9. Sequence of salinity sections from shipboard hydrographic transects in Aug 1994. The salinity scale is shown next to the 12 Aug panel.

north and south of the central line support this view. The low-salinity water in the numerical model results of Fong and Geyer (2001) also persisted as coherent lenses.

The buoyant coastal plume response described above is far more complicated than either the numerical model simulations or the simple theory for a variety of reasons that include variable winds with reversals, variable ambient shelf currents and stratification, more complex bathymetry, and multiple buoyant current events that can, for example, merge. Additionally, the relevance of a two-dimensional perspective, used in both the theory and the description of the observations, is not clear. The alongshore displacement during the 12-day period estimated from the observed alongshore current is about 60 km, less than the alongshore extent of the buoyant coastal plumes. This explains why the low-salinity lenses are not swept out of the observational domain. Despite these limitations, predictions from the theory proposed in section 2 are compared with the observations for the 12-day period in August described above.

To apply the theory with realistic wind forcing required several modifications. Besides the continual entrainment at the offshore edge of the plume, intermittent entrainment may occur over the entire plume in response to increases in the wind stress. The equations are time stepped using the hourly wind observations. At the start of each time step, increases in plume thickness due to increases in the wind stress magnitude are accounted for by setting $h(t)$ to the maximum of h from the previous time step and an updated estimate of h from (15) using the new wind stress magnitude. Entrainment is assumed to occur at the onshore edge of the plume during reversals to downwelling-favorable winds if the plume is detached from the coast. While it is straightforward to include a sloping bottom in the model, this was not done because the region onshore of where the front intersects the bottom is narrow for the Chesapeake plume; that is, the Chesapeake plume tends to be ‘‘surface trapped’’ based on the criterion of Lentz and Helfrich (2002). The time-stepping model was checked by comparing calculations for a constant upwelling-favorable wind stress with the analytic expressions in section 2. The two approaches gave essentially identical results.

The theoretical model was initialized with observations from the 11 August salinity and density sections, $h_i = 8$ m, $W_i = 7$ km, and $\Delta\rho_i = 5$ kg m^{-3} (Fig. 9), and then forced with the observed wind stress (Fig. 8a). Time series of h, $\Delta\rho$, W, and X from the theory compare reasonably well to estimates from the ship transects (Fig. 10). The theory accurately reproduces both the increase in plume thickness and the decrease in plume density. There are only four observations of W and X because many of the transects did not extend far enough offshore to sample the entire plume (Fig. 9). The theory appears to overestimate X and W on 19 and 21 August. However, the observations of W and X on 19 and 21 August are lower bounds because the offshore edge of the plume

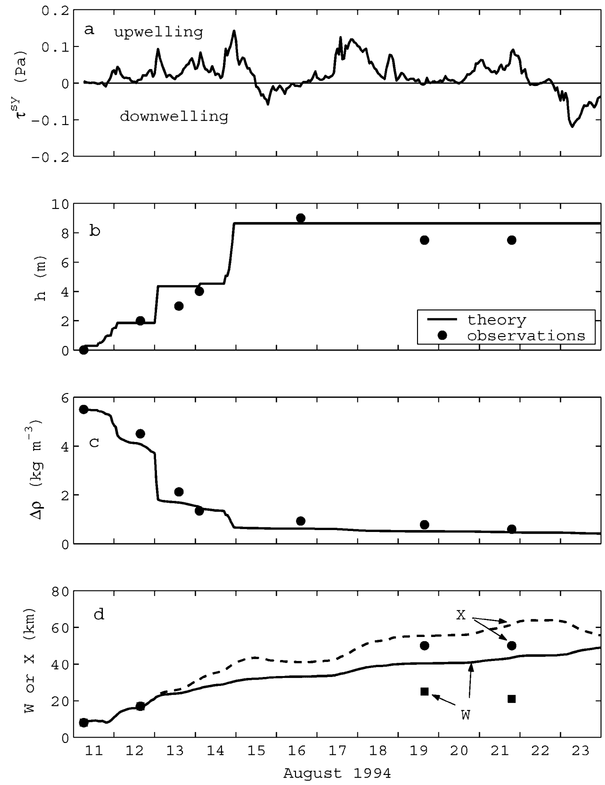

FIG. 10. Comparisons of theoretical estimates (lines) and observations (symbols) of (b) buoyant plume thickness h, (c) density anomaly $\Delta\rho$, and (d) width W and offshore position X for a period in Aug when wind stresses, shown in (a), were primarily upwelling-favorable (positive values). Values of X and W on 19 and 21 Aug may be larger than shown because the buoyant plume extended beyond the offshore extent of the ship transect (see Fig. 9).

again extended beyond the survey (maximum offshore distance about 48 km); thus the actual values of W and X may be larger. The general agreement between the theory and the August observations suggests that the two-dimensional model is relevant to this period and provides indirect evidence for the assumed entrainment process.

It is interesting to contrast the theoretical estimates for the Chesapeake plume with estimates from a larger plume such as the Mississippi River plume. For a moderate, upwelling wind stress of 0.1 Pa and the initial conditions listed above for the Chesapeake plume, $h_s = 2.2$ m, $t_s = 18$ h, and $t_{sep} = 5$ h. In contrast, for the same wind stress, using $h_i = 15$ m, $W_i = 40$ km, and $\Delta\rho_i = 5$ kg m^{-3} for the Mississippi River (inferred from Fig. 4 in Wiseman et al. 1997) yields $h_s = 1.6$ m, $t_s = 7$ days, and $t_{sep} = 4$ days. While h_s is similar for the two plumes because the wind stress and density anomalies are the same, the time scales differ by an order of magnitude because the cross-sectional areas differ by an order of magnitude. For the Chesapeake, both t_s and t_{sep} are similar to the time scale of a typical wind event. This implies that a single wind event can cause the

Chesapeake plume to separate from the coast and the associated entrainment can double the plume volume. Since the density anomaly scales as $(1 + \hat{t})^{-1}$, it takes a 0.1-Pa upwelling wind stress about a week to decrease the Chesapeake plume density to 10% of its original value. For the Mississippi plume, both t_s and t_{sep} are longer than a typical wind event, which may explain why the Mississippi plume persists as a buoyant coastal plume for much of the year, except in mid-to-late summer when persistent upwelling-favorable winds move the low-salinity water toward the east (Cochrane and Kelly 1986; Wiseman et al. 1997; Li et al. 1997). Furthermore, the theoretical estimate suggests it would take months for an upwelling wind stress of 0.1 Pa to reduce the density anomaly of the Mississippi plume to 10% of its initial value. This comparison suggests that buoyant plumes similar to or smaller than the Chesapeake plume should be strongly influenced by wind forcing on the synoptic time scale of a day or two, while much larger plumes, such as the Mississippi plume, should be more strongly influenced by wind forcing on monthly to seasonal time scales.

5. Summary

A simple, two-dimensional theory for the response of a buoyant coastal plume to upwelling-favorable winds is developed to gain insight into this process, particularly the associated entrainment. This theory builds on a conceptual model developed by Fong and Geyer (2001) and insights gained from their numerical model results. The key assumption is that entrainment occurs at the offshore edge of the buoyant plume in the region where the isopycnals shoal to intersect the surface. In this region, continual entrainment is assumed to be a result of a competition between geostrophic adjustment associated with the buoyancy force and wind-driven mixing. The two-dimensional theory based on this assumption, combined with an oversimplified triangular geometry and a bulk Richardson number criterion, provides estimates of the time-dependent plume density, thickness, width, offshore position, and the entrainment rate in response to an upwelling wind stress, given the initial plume density, width, and thickness, the Coriolis parameter, a critical value for the bulk Richardson number, and the wind stress.

There are two key parameters derived from the theory: a thickness scale h_s and a time scale t_s. The normalized thickness scale $\tilde{h}_s$ may be thought of as a Froude number that determines the plume response to the onset of the wind stress. If $\tilde{h}_s \geq 1$, the wind forcing is strong enough for entrainment to occur over the entire extent of the plume and the plume thickness at the onset of the wind forcing is h_s. If $\tilde{h}_s < 1$, only a portion of the plume is thin enough for entrainment to occur, and the plume thickness at the onset of the wind forcing is larger than h_s.

The subsequent evolution of the plume after the onset of the wind forcing depends on the time scale $t_s = 2A_o/(\sqrt{\mathrm{Ri}_c}U_E)$, the time for entrainment to double the cross-sectional area A_o after the onset of the wind forcing, where U_E is the Ekman transport. Normalizing time by t_s, the plume thickness increases as $(1 + \hat{t})^{1/3}$ and the width as $(1 + \hat{t})^{2/3}$, and so the cross-sectional area increases as $(1 + \hat{t})$. Since the plume buoyancy anomaly is conserved, the density anomaly decreases as $(1 + \hat{t})^{-1}$. The average entrainment rate over the plume $\overline{w}_e$ scales as $(1 + \hat{t})^{-2/3}$. The time that it takes the buoyant plume to separate from the coast t_{sep} depends on t_s and h_s. For $\tilde{h}_s \geq 1$, the plume is assumed to separate from the coast immediately, that is, in a time scale of f^{-1} or less, since the theory neglects the spinup time of the Ekman response. As $\tilde{h}_s$ decreases, that is, for weaker wind stress, t_{sep} becomes increasingly large. Once the plume separates from the coast, it will move in response to the wind forcing and ambient shelf flow, but it should not propagate alongshore as a buoyant gravity current.

The theory accurately reproduces the numerical model results of Fong and Geyer (2001), including their estimates of the plume-average entrainment rate $\overline{w}_e$, though the regression coefficient was 1.7 for $\overline{w}_e$ (Table 1 and Figs. 4–6). The agreement suggests that the theory provides insight into the physics represented by the numerical model results. In particular, the hypothesized entrainment process is a reasonably accurate description of the entrainment process occurring in the numerical model. The theory also reproduces the observed response of the buoyant plume from Chesapeake Bay to weak upwelling-favorable winds during a 12-day period in August 1994, suggesting that it is relevant to the oceanic response. Further observations are needed to assess the usefulness and limitations of this simple theory for understanding the response of buoyant coastal plumes to upwelling winds. Observations of the response of buoyant plumes having different scales, such as the Mississippi plume, are needed to evaluate the proposed ideas. Direct estimates of both entrainment rates using, for example, dye or by making turbulent salt flux measurements would be particularly insightful to determine where and when entrainment occurs.

Acknowledgments. I greatly appreciate Derek Fong's helpfulness and patience in answering my numerous questions regarding his numerical modeling results. John Largier graciously provided the shipboard hydrographic data presented in section 4. Dave Chapman, Derek Fong, Rich Garvine, Robert Hetland, Jim Lerczak, and Peter Windsor provided constructive comments on an early draft of this manuscript. This work was funded by the National Science Foundation under Grants OCE-0095059 and OCE-0241292.

REFERENCES

Alessi, C. A., S. J. Lentz, and J. Austin, 1996: Coastal Ocean Processes Inner-Shelf Study: Coastal and moored physical oceanographic measurements. Tech. Rep. WHOI-96-06, Woods Hole Oceanographic Institution, Woods Hole, MA, 142 pp.

Austin, J. A., and S. J. Lentz, 1999: The relationship between synoptic weather systems and meteorological forcing on the North Carolina inner shelf. *J. Geophys. Res.,* **104,** 18 159–18 186.

Berdeal, I. G., B. M. Hickey, and M. Kawase, 2002: Influence of wind stress and ambient flow on a high discharge river plume. *J. Geophys. Res.,* **107,** 3130, doi:10.1029/2001JC000932.

Chao, S.-Y., 1988: River-forced estuarine plumes. *J. Phys. Oceanogr.,* **18,** 72–88.

Cochrane, J. D., and F. J. Kelly, 1986: Low-frequency circulation on the Texas–Louisiana continental shelf. *J. Geophys. Res.,* **91,** 10 645–10 659.

Donato, T. F., and G. O. Marmorino, 2002: The surface morphology of a coastal gravity current. *Cont. Shelf Res.,* **22,** 141–146.

Fong, D. A., and W. R. Geyer, 2001: Response of a river plume during an upwelling favorable wind event. *J. Geophys. Res.,* **106,** 1067–1084.

——, ——, and R. P. Signell, 1997: The wind-forced response of a buoyant coastal current: Observations of the western Gulf of Maine plume. *J. Mar. Syst.,* **12,** 69–81.

Hallock, Z. R., and G. O. Marmorino, 2002: Observations of the response of a buoyant estuarine plume to upwelling favorable winds. *J. Geophys. Res.,* **107,** 3066, doi:10.1029/2000JC000698.

Hickey, B. M., L. J. Pietrafesa, D. A. Jay, and W. C. Boicourt, 1998: The Columbia River Plume Study: Subtidal variability in the velocity and salinity fields. *J. Geophys. Res.,* **103,** 10 339–10 368.

Houghton, R. W., C. E. Tilburg, R. W. Garvine, and A. Fong, 2004: Delaware River plume response to a strong upwelling-favorable wind event. *Geophys. Res. Lett.,* **31,** L07302, doi:10.1029/2003GL018988.

Johnson, D. R., A. Weidemann, R. Arnone, and C. O. Davis, 2001: Chesapeake Bay outflow plume and coastal upwelling events: Physical and optical properties. *J. Geophys. Res.,* **106,** 11 613–11 622.

——, J. Miller, and O. Schofield, 2003: Dynamics and optics of the Hudson River outflow plume. *J. Geophys. Res.,* **108,** 3323, doi:10.1029/2002JC001485.

Kourafalou, V. H., L.-Y. Oey, J. D. Wang, and T. N. Lee, 1996: The fate of river discharge on the continental shelf, 1, Modeling the river plume and the inner shelf coastal current. *J. Geophys. Res.,* **101,** 3415–3434.

Large, W. G., and S. Pond, 1981: Open ocean momentum flux measurements in moderate to strong winds. *J. Phys. Oceanogr.,* **11,** 324–336.

Lentz, S. J., and K. R. Helfrich, 2002: Buoyant gravity currents along a sloping bottom in a rotating frame. *J. Fluid Mech.,* **464,** 251–278.

——, R. T. Guza, S. Elgar, F. Feddersen, and T. H. C. Herbers, 1999: Momentum balances on the North Carolina inner shelf. *J. Geophys. Res.,* **104,** 18 205–18 226.

——, S. Elgar, and R. T. Guza, 2003: Observations of the flow field near the nose of a buoyant coastal current. *J. Phys. Oceanogr.,* **33,** 933–943.

Li, Y., D. Nowlin Jr., and R. O. Reid, 1997: Mean hydrographic fields and their interannual variability over the Texas–Louisiana continental shelf in spring, summer, and fall. *J. Geophys. Res.,* **102,** 1027–1049.

Lohrenz, S. E., C. L. Carroll, A. D. Weidemann, and M. Tuel, 2003: Variations in phytoplankton pigments, size structure and community composition related to wind forcing and water mass properties on the North Carolina inner shelf. *Cont. Shelf Res.,* **23,** 1447–1464.

McGillicuddy, D. J., Jr., R. P. Signell, C. A. Stock, B. A. Keafer, M. D. Keller, R. D. Hetland, and D. M. Anderson, 2003: A mechanism for offshore initiation of harmful algal blooms in the coastal Gulf of Maine. *J. Plankton Res.,* **25,** 1131–1138.

Mellor, G. L., and T. Yamada, 1982: Development of a turbulence closure model for geophysical fluid problems. *Rev. Geophys. Space Phys.,* **20,** 851–875.

Pollard, R. T., P. B. Rhines, and R. O. R. Y. Thompson, 1973: The deepening of the wind-mixed layer. *Geophys. Fluid Dyn.,* **3,** 381–404.

Rennie, S., J. L. Largier, and S. J. Lentz, 1999: Observations of low-salinity coastal current pulses downstream of Chesapeake Bay. *J. Geophys. Res.,* **104,** 18 227–18 240.

Sanders, T. M., and R. W. Garvine, 2001: Fresh water delivery to the continental shelf and subsequent mixing: An observational study. *J. Geophys. Res.,* **106,** 27 087–27 101.

Selby, S. M., 1973: *Standard Mathematical Tables.* The Chemical Rubber Company Press, 714 pp.

Trowbridge, J. H., 1992: A simple description of the deepening and structure of a stably stratified flow driven by a surface stress. *J. Geophys. Res.,* **97,** 15 529–15 543.

Waldorf, B. W., J. L. Largier, S. Rennie, J. Austin, and C. Greengrove, 1995: Coastal ocean processes (CoOP) pilot project data report: R/V *Cape Hatteras* shipboard measurements; Underway, CTD, and ADCP data, August 1994. Tech. Rep. SIO Reference Series 95-29, Scripps Institution of Oceanography, La Jolla, CA, 419 pp.

——, ——, ——, and ——, 1996: Coastal Ocean Processes (CoOP) pilot project data report: R/V *Cape Hatteras* shipboard measurements; Underway, CTD, and ADCP data, October 1994. Tech. Rep. SIO Reference Series 96-9, Scripps Institution of Oceanography, La Jolla, CA, 407 pp.

Wang, D. P., 1979: Low frequency sea level variability on the Middle Atlantic Bight. *J. Mar. Res.,* **37,** 683–697.

Whitney, M. M., and R. W. Garvine, 2004: Wind influence on a coastal buoyant outflow. *J. Geophys. Res.,* in press.

Wiseman, W. J., N. N. Rabelais, R. E. Turner, S. P. Dinnel, and A. MacNaughton, 1997: Seasonal and interannual variability with the Louisiana coastal current: Stratification and hypoxia. *J. Mar. Syst.,* **12,** 237–248.

Xing, J., and A. M. Davies, 1999: The effect of wind direction and mixing upon the spreading of a buoyant plume in a non-tidal regime. *Cont. Shelf Res.,* **19,** 1437–1483.